

New modes of FFT impedance spectroscopy applied to semiconductor pore etching and materials characterization

J. Carstensen, E. Foca, S. Keipert, H. Föll, M. Leisner, and A. Cojocaru

Chair for General Materials Science, Faculty of Engineering, Christian-Albrechts-University of Kiel, Kaiserstr. 2, 24143 Kiel, Germany

Received 24 January 2008, revised 27 May 2008, accepted 16 July 2008
 Published online 18 September 2008

PACS 81.05.Cy, 81.05.Ea, 81.05.Rm, 82.47.Wx, 84.37.+q

A systematic approach for the application of fast Fourier transform (FFT) impedance spectroscopy to semiconductor photo-electrochemistry is given. In particular, photo-impedance spectroscopy in two novel modes is used in conjunction with conventional current–voltage impedance spectroscopy, and applied to some aspects of pore etching in InP and Si as well as to the characterization of multicrystalline Si or other solar cell material. The technique, applicable in situ with high time resolution, employs optimized hardware and software, extensive mathematical modeling of carrier transport, and the numerical implementation of fast parameter extraction algorithms. The complete system with a fully integrated impedance spectrometer delivers a wealth of new data including key parameters of pore etching. Examples given include the in situ tracking of the fast switch-over between pore growth modes in InP as well as following a pore etching

process over long time scales in Si. FFT impedance spectroscopy in the novel back side illumination mode, in combination with the conventional mode, allows not only some active control of macropore etching in n-type Si by supplying crucial real-time data like the valence of the dissolution process and the pore depth, but also provides new fundamental insights into the electrochemical processes occurring at the (porous) electrode. FFT photo-impedance spectroscopy in the front side illumination mode used in conjunction with a scanned laser beam allows fast local measurements of all semiconductor parameters relevant for solar cell applications, like doping concentration, minority carrier lifetime, diffusion constant, or surface recombination velocity with high spatial resolution; this is demonstrated for large multicrystalline Si wafers.

phys. stat. sol. (a) 205, No. 11, 2485–2503 (2008) / DOI 10.1002/pssa.200824033

New modes of FFT impedance spectroscopy applied to semiconductor pore etching and materials characterization

Feature Article

J. Carstensen, E. Foca, S. Keipert, H. Föll, M. Leisner, and A. Cojocaru*

Chair for General Materials Science, Faculty of Engineering, Christian-Albrechts-University of Kiel, Kaiserstr. 2, 24143 Kiel, Germany

Received 24 January 2008, revised 27 May 2008, accepted 16 July 2008
Published online 18 September 2008

PACS 81.05.Cy, 81.05.Ea, 81.05.Rm, 82.47.Wx, 84.37.+q

* Corresponding author: e-mail ac@tf.uni-kiel.de, Phone: +49 431 880 6180, Fax: +49 431 880 6178

A systematic approach for the application of fast Fourier transform (FFT) impedance spectroscopy to semiconductor photo-electrochemistry is given. In particular, photo-impedance spectroscopy in two novel modes is used in conjunction with conventional current–voltage impedance spectroscopy, and applied to some aspects of pore etching in InP and Si as well as to the characterization of multicrystalline Si or other solar cell material. The technique, applicable in situ with high time resolution, employs optimized hardware and software, extensive mathematical modeling of carrier transport, and the numerical implementation of fast parameter extraction algorithms. The complete system with a fully integrated impedance spectrometer delivers a wealth of new data including key parameters of pore etching. Examples given include the in situ tracking of the fast switch-over between pore growth modes in InP as well as following a pore etching

process over long time scales in Si. FFT impedance spectroscopy in the novel back side illumination mode, in combination with the conventional mode, allows not only some active control of macropore etching in n-type Si by supplying crucial real-time data like the valence of the dissolution process and the pore depth, but also provides new fundamental insights into the electrochemical processes occurring at the (porous) electrode. FFT photo-impedance spectroscopy in the front side illumination mode used in conjunction with a scanned laser beam allows fast local measurements of all semiconductor parameters relevant for solar cell applications, like doping concentration, minority carrier lifetime, diffusion constant, or surface recombination velocity with high spatial resolution; this is demonstrated for large multicrystalline Si wafers.

© 2008 WILEY-VCH Verlag GmbH & Co. KGaA, Weinheim

1 Introduction Impedance spectroscopy is an old and valued tool for the investigation of the kinetics of electrode reactions in electrochemistry. Its basic principles as well as its range of applications have been covered in a dedicated textbook [1] and will not be addressed here.

The topic of this paper is mostly the application of impedance spectroscopy to semiconductor electrochemistry, in particular to that subset of semiconductor electrochemistry that has to do with pore formation or pore etching and solar material characterization. Having made this clarification, the first topics that need to be addressed are the particular requirements that must be met if impedance spectroscopy is to be used in the context of pore etching in semiconductors. This is not a trivial topic as witnessed by

the fact that after 20 years of pore etching, impedance spectroscopy so far has hardly been used to investigate the many open questions of this large and growing branch of semiconductor electrochemistry. For basic literature about pore etching in semiconductors, the reader is referred to the two books dedicated to this issue [2, 3], to four conference proceedings [4–7], to review papers of the authors' group [8, 9], as well as to reviews of Smith and Collins [10], Ossicini and co-workers [11, 12], and the articles of Lehmann et al. [13] and Chazalviel et al. [14].

Some modes of pore etching in Si (and to a lesser extent in other semiconductors) require the illumination of the electrode, usually the back side of the sample. In particular, back-side illumination (bsi) is the decisive factor

for etching well-defined macropores into n-type Si substrates in aqueous HF-based electrolytes; so-called n-Si-macro(aqu, bsi) pores in the self-explanatory short-hand notation introduced in [8], which we shall use throughout this paper. However, n-Si-macro(aqu, fsi) pores (fsi = front-side illumination) have been investigated to some extent, too [15], as well as n-Ge-macro(aqu, bsi) pores [16], not to mention pore types that do not need illumination, e.g. p-Si-macro(org) pores, (org = electrolytes based on organic solvents), p-Si-micro(aqu) pores, n⁺-, p⁺-Si-meso(aqu) pores, or n-(III–V)-macro/meso pores. As long as illumination is used for pore formation, the possibility of using ‘photo-impedance’ spectroscopy exists, meaning here that the light intensity P is modulated and the response in the current I is measured – a mode that we will call PI (photo-impedance) here for short (note that in [17–24] other terms have been used in comparable contexts).

This paper deals with the two possible PI modes, i.e. bsi-PI or fsi-PI, and the conventional voltage–current impedance mode (UI mode for short) where the applied voltage U is modulated and the response in the current I is measured. As it turns out, the two PI modes are quite different from the UI mode; not only as far as their experimental implementation is concerned but in particular in the interpretation of the spectra obtained. This allows quite different and rather useful ranges of applications in comparison to the UI mode. It will be shown that the bsi-PI mode in conjunction with the UI mode allows in situ monitoring of many, if not all, n-Si-macro(aqu, bsi) pore etching parameters, in particular the pore depth d_p and the valence n of the dissolution process, and thus opens the way to in situ active control of pore etching, or quick assessments of

electrolytes. The UI mode by itself, applied to pore etching modes not needing illumination, can still give useful information in the general context of pore etching; this will be demonstrated for the case of pores in InP, which show a particularly complex (and so far not well understood) behavior.

While voltage or UI impedance is a widely used technique, PI is fairly new. A few previous papers mention fsi-PI [17, 18, 21–23] but nothing has been published previously on bsi-PI. The fsi-PI mode, while applicable to photo-electrochemistry in general and macro/meso(fsi) pores in particular, has not yet been used for this. However, it is also of interest for characterizing basic electrode properties under conditions where the working electrode is just used as the absorber part of an electrochemical or solid-state solar cell. That is because a reversely biased semiconductor–electrolyte junction under front-side illumination is quite similar to a solar cell. The only difference to a solid-state solar cell is found in the precise nature of the junction – but this will, in a first approximation, only change the open circuit voltage U_{OC} (and possibly the leakage currents) but not the short circuit current I_{SC} , or more precisely the reverse saturation current, which is completely dominated by the electrode properties (at least for electrodes suitable for making solar cells with efficiencies above a few percent). In a second approximation this statement would have to be modified to some extent, but for the purposes of this paper it is sufficient to appreciate that the fsi-PI mode, originally developed for semiconductor–electrolyte junctions, can just as well be applied not only to the whole area of a solar cell but, via laser beam scanning, to individual pixels of, for example, large-area standard Si solar cells. It will be shown that this ‘scanning fsi-PI spectroscopy’ can provide an unprecedented wealth of quantitative local data, including parameters hitherto not obtainable, with respect to the solar cell material and related process issues.

It is one thing to measure a (typically noisy) in situ impedance spectrum, and another thing to interpret the resulting data. Three (interconnected) tiers of interpretation might be distinguished, as they will arise in this paper. First, just looking at Nyquist or Bode plots of the data, some general interpretation is possible. What kinds of typical semicircles are observed and how many? Are there straight lines typical for Warburg impedances and thus diffusion limitations of some process? What kind of time constants are involved and which processes ‘die out’ at higher frequencies? Second, an impedance model (sometimes represented as equivalent circuit diagram) can be conceived with components that give the best match to the measured data. In a somewhat more abstract but related approach, standard equations for certain types of processes can be used, e.g. processes involving at least two or three different time constants. If the equations chosen match the spectra, the parameters contained in the equations can be extracted. That is, perhaps, the most ubiquitous standard procedure, and it is rather powerful as long as it is sufficiently clear



Jürgen Carstensen was born in Flensburg, Germany, in 1964. He began his studies in physics at the Christian-Albrechts-University of Kiel 1984 and received his Ph.D. from the Institute of theoretical physics in 1993 for work on superconductivity. Subsequently, he joined the group of Prof. Helmut Föll at the Institute for materials science at the Christian-Albrechts-University of Kiel as a research associate.

He began his work employing semiconductor electrochemistry for the mapping of minority carrier life-time in solar cell substrates and in the emerging field of porous semiconductors and related self-organization phenomena. He was instrumental in developing the unique ‘CELLO’ and ‘CELLOplus’ measurement techniques capable of mapping nearly all of the important solar cell parameters with good local resolution. He has co-authored more than 120 papers.

what the components of the relevant equations signify in terms of the electrochemical reactions and the relaxation/transport phenomena that are occurring. Both approaches will be used in this paper, but a third approach, used here in a novel way, is the decisive one. In this approach the whole 'history' of the relevant charge carriers (always holes in the n-type semiconductor treated here) is obtained by solving the proper time-dependent diffusion equation (including generation and recombination terms) for the new PI modes. The theoretical impedance obtained in this way thus depends on the most basic parameters of the material. As will be shown, matching the theoretically obtained impedance to the measured data then allows one to extract quantitatively up to eleven system parameters. Mixed forms are possible, too, and will be demonstrated.

It is worth mentioning in this context that earlier applications of the newly developed fsi-PI mode always produced data that resisted any reasonable interpretation. The reason was that the spectra always included some resonant processes that could not be significant for the materials under investigation; nor was it possible to separate them from the ones that characterized the system under investigation. Nevertheless, a consistent interpretation of the data is now possible, if certain peculiarities of the total system are considered, and this paper will show how that is done. Some short preliminary papers elucidating parts of the topics dealt with in this detailed overview can be found elsewhere [15, 25, 26].

2 Special topics for conventional impedance and PI in the context of semiconductor electrochemistry The application of any impedance spectroscopy mode to semiconductor electrochemistry, subset pore etching, encounters a number of specific conditions tied to pore etching that must be considered if useful impedance spectra are to be obtained. These are:

1. Pore etching almost always implies that samples of single-crystalline semiconductors are used in sizes from at least a few mm² (most researchers use 100 mm² for Si) up to 30,000 mm² typical for 200 mm ('8-inch') standard wafers [8].

2. The electrochemical reactions producing pores (i.e. the reactions that dissolve most of the semiconductor) by definition occur mostly at the pore tips (= active areas), i.e. only in parts of the total sample surface area. As a consequence, the ratio of active areas to the total area decreases monotonically with time since pore growth generates new passive surfaces.

3. The primary pore etching process may be very sensitive to some etching parameters, e.g. the flow rate of the electrolyte or the temperature, but rather insensitive to others. Small variations of the potential for example may only produce very small current responses.

4. Conditions at a pore tip necessarily change with the pore depth if the external parameters are not changed accordingly. In particular, the concentration of educts and

products at the pore tip will change with increasing pore depth, both due to the necessity to have large concentration gradients to drive the required diffusion currents into or out of the growing pore. The potential at the pore tips also decreases with increasing pore depth because of ohmic losses in the pore, and so on. Obvious measures to counter any one of these effects usually lead to unwanted changes of other parameters.

5. Many self-ordering effects may be encountered, often turning on or off without obvious reasons, cf. [8, 27, 28], emphasizing point (3) above once more. Quite often these self-ordering effects are accompanied by (or are simple expressions of) self-induced current and/or potential oscillations occurring everywhere or just in parts of the sample. These oscillations may easily interfere with all modes of impedance spectroscopy in non-trivial ways.

Using standard UI impedance spectroscopy without special precautions under these conditions will almost certainly produce meaningless data. In particular, if the etching is not very uniform, the impedance data represent some (weighted) average over locally different kinds of reactions at pore tips and pore walls. This is a considerable problem for large-area etching, where it might be difficult to achieve uniform electrolyte flow or uniform back-side contacts and thus uniform pore growth conditions, as well as for small samples, because the then non-negligible area close to the O-ring usually shows an etching behavior quite different from the inner parts. A definite 'must' for impedance spectroscopy during pore growth is to obtain a complete spectrum very fast in order to ensure quasi-static conditions during a measurement that often is made in a very dynamic environment. Pore growth in InP, for example, may switch between completely different growth modes within fractions of a second – either self-organized or by simple external stimuli. The pores in this case grow with a speed of up to 10 μm/min, with a concomitant monotonic increase of the ohmic losses inside a pore and changes of the diffusion conditions, and this leads to an unacceptable drift if the time to measure a complete impedance spectrum takes more than a few seconds. In addition, the modulation amplitude of the input parameter (potential or light intensity in the cases treated here) has to be kept as small as possible to allow for linear response of the system and undisturbed pore growth.

To cut a long story short, we have found that using fast Fourier transform (FFT) impedance spectroscopy in all three modes was one of the keys to success. The instrumentation used is custom made [29] and described elsewhere in some detail [30, 31]. One important feature of this approach is the easy possibility for data validation [32]. It is optimally interfaced with the etching equipment (typically from ET&TE) and spectra in all three modes are taken within 0.6 s in a frequency range of typically 5 Hz to 20 kHz. Modulation in all cases was produced by superimposing several sinusoidal signals with identical amplitudes.

If either mode of PI is to be used, the intensity of the light source needs to be modulated at all required frequencies with a constant (small) amplitude. This is next to impossible with regular light sources; throughout this work, therefore, only light-emitting diode (LED) arrays (or, in the case of solar cells, a laser) have been employed.

The present equipment allows one to obtain more than 1000 complete impedance spectra per hour; during an n-Si-macro(aqu, bsi) etching experiment lasting up to 15 h, thousands of UI and PI spectra result with a total data volume of >10 GB.

The hardware used ensures that the mandatory conditions for any IS measurement (system is in a steady state and responds linearly) can be met. Non-steady state during the (1 s) measurement leads to large drifts between spectra and thus is easily detected. Non-linear response leads to peaks at ‘wrong’ frequencies in a response–frequency plot that is easily seen on the screen or even detected automatically. The total amplitude of the modulation in an FFT mode is always larger than the amplitudes of the individual signals, so this point is of some importance here. In what follows only data from measurements that meet the above conditions are shown. The precise experimental details are given in the context of the application examples in what follows.

3 Application of UI FFT impedance spectroscopy to pore etching in InP It can be argued that the understanding of self-induced or externally induced sharp transitions from so-called crystallographic pores (‘crysto’ pores) to current-line oriented pores (‘curro’ pores) in InP as described in [33, 34] poses one of the biggest challenges in the field of semiconductor electrochemistry. Figure 1 shows paradigmatic examples from [33]. In the upper part of Fig. 1a curro pores are visible; in the lower half crysto pores extending in both possible downward $\langle 111\text{B} \rangle$ directions are expressed. The transition was induced by a reduction of the potential and thus of the current density; note that it is very sharp in space (and therefore also time). Figure 1b shows a curro–crysto–curro transition induced by simply turning off the current for about 1 s. Note that this short interruption suffices to erase completely the ‘memory’ of the pore growth mode in the upper half of the figure. The pores first continue to grow in the crysto mode, followed by a self-induced switch to curro pores a short time later. The transition thus can be called ‘sharp’ in time and space with some justification.

Besides some qualitative arguments given in [9], no attempt has been made to explain this peculiar feature that by now has also been observed to occur in a similar way in Si [35] and GaP [36] but not (yet) in Ge or GaAs. While we will not yet go beyond our earlier attempts at understanding this behavior as given in [37], we will present the first impedance data obtained during this transition, mostly in order to illustrate the remarks made in Section 2. The pores produced during the measurements shown here were etched using a viscous electrolyte obtained by adding car-

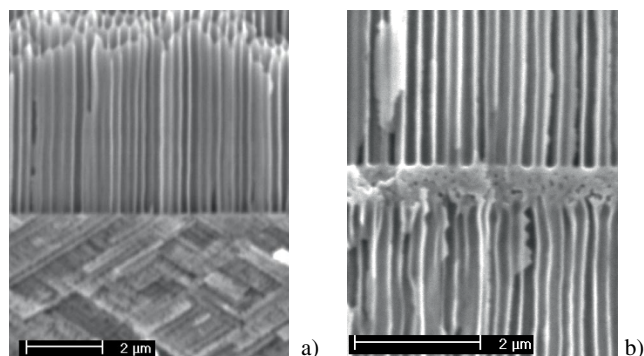


Figure 1 Illustration of the curro–crysto switchover in InP. a) Externally induced switchover from curro pores (top) to crysto pores. b) Switchover from curro to crysto and (self-induced) back to curro pores by turning off the current for 1 s.

boxymethylcellulose sodium salt. This measure slows down the dynamics of the system to some extent without changing the general behavior, and thus allows one to follow the process by taking impedance spectra at 1 s intervals.

Figure 2 shows typical impedance data obtained with UI FFT impedance spectroscopy employed in situ during repeated switches between crysto and curro pores that were induced by switching the applied potential between 2 V and 10 V as shown in Fig. 2a (top); the resulting pore structure is a multilayered sequence of crysto–curro pores similar to the one shown in Fig. 1 or in, for example, [9]. The modulation amplitudes of individual frequencies were typically 3 mV. Etching conditions were nearly identical to those described in detail in [9], the most important data are: n-type, doping concentration = $5.4 \times 10^{17} \text{ cm}^{-3}$, $\{100\}$ orientation, aqueous 5 wt% HCl-based circulated electrolyte; potential and currents as indicated; sample size = 25 mm^2 ; temperature of the electrolyte controlled to $\pm 0.1 \text{ }^\circ\text{C}$. Using such small samples at high current densities will usually result in significant differences of the pore morphologies near the O-ring; impedance data then reflect some average of ‘border’ and ‘main body’ data that cannot easily be separated. As far as possible it has been ascertained that the impedance data shown mainly reflect the etching conditions in the still large homogeneously etched center part of the cell.

Without going into details, the three semicircles obtained (somewhat distorted because of different scales on the axes) illustrate that at least three processes with different time constants are involved, and that there are considerable changes in the relative strength of these processes over time, in particular during periods where crysto pores are growing, which are not expressed in the immediate pore morphology. A Nyquist plot with the complexity as illustrated in Fig. 2 needs at least three resistances and three time constants for adequate fitting. Following general schemes as, for example, outlined in [1], a model has been found, which allows one to fit the impedance data very well

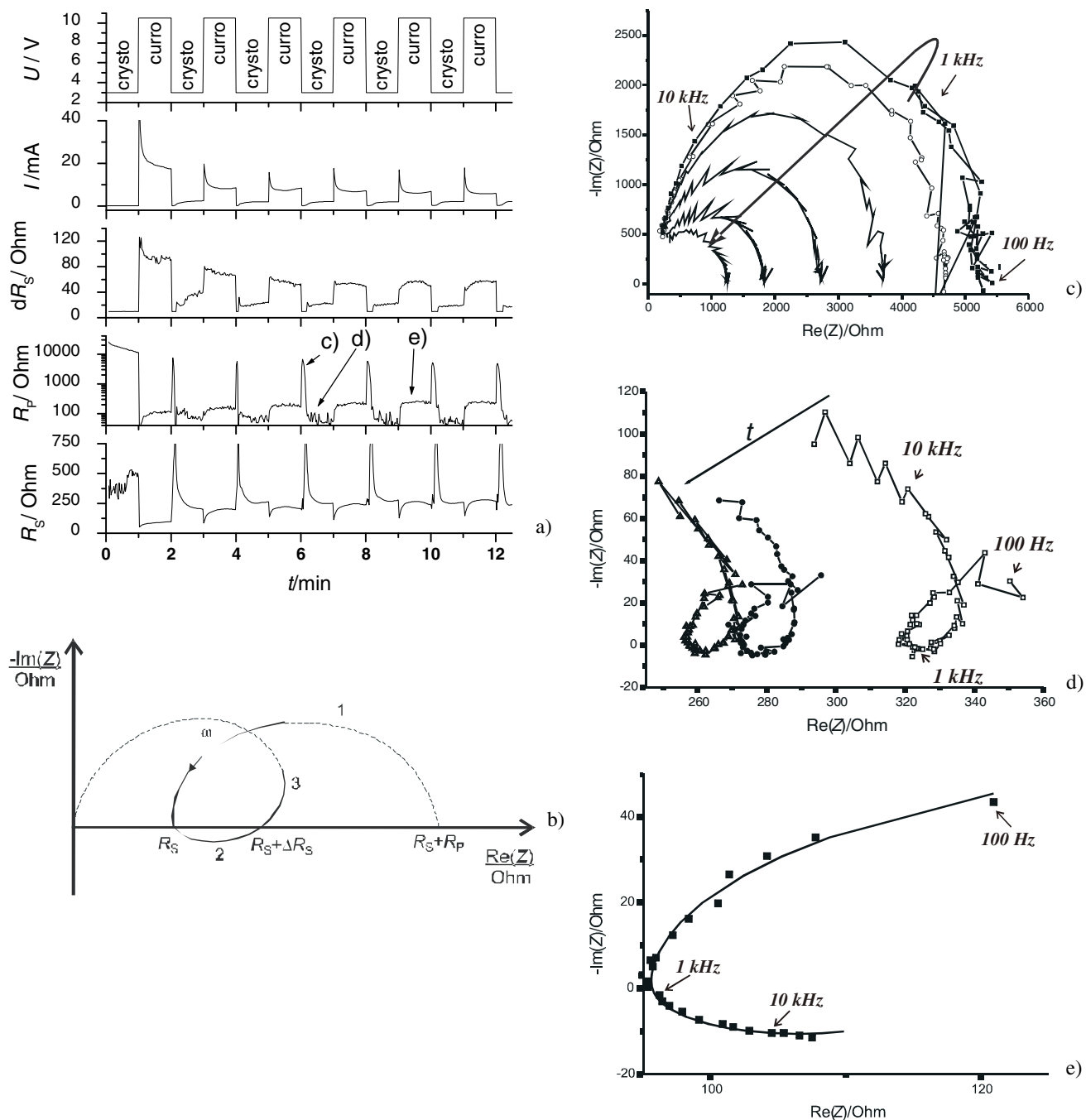


Figure 2 a) Preset potential vs. time curve and resulting time dependence of current and the resistance fitting parameters according to Eq. (1). The impedance measurements have been conducted at intervals of 1 s in a frequency range between 10 Hz and 40 kHz, containing 27 frequencies. b) Schematic Nyquist plot for the model expressed in Eq. (1). c) Examples for the measured Nyquist plots in the transition regime from curro to crysto pores as marked in (a). The lines are guides to the eye. The transition takes place at the maximum R_p value. The individual spectra were taken successively with 2 s intervals and illustrate the strong decrease of R_p in this phase. d) Continuations of the Nyquist plots from (c) on a different scale and in the stable crysto pore phase (marked also in (a)), illustrating the continuous decrease of R_s while R_p stays nearly constant. The lines are guides to the eye. e) Example for a Nyquist plot in the stable curro pore phase (marked also in (a)): squares, measured; line, fit. In this phase none of the resistances changes significantly so all impedance data look much the same.

in the cristo and current pore growth mode as well as in the transition regime:

$$Z_{\text{complete}}(\omega) = \frac{1}{\frac{1}{R_p} + i\omega C_p} + \frac{1}{\frac{1}{R_s} \frac{1}{1+i\omega\tau} + \frac{1}{R_s + \Delta R_s} \frac{1}{1+i\omega\tau} + i\omega C_s}. \quad (1)$$

The names of the fitting parameters have been chosen to be consistent with those that will come up in Eq. (2), although it is not clear that, for example, R_s is really a serial resistance. The first term in Eq. (1) describes an electrochemical reaction with a transfer resistance R_p and an interface capacitance C_p (cf. semicircle 1 in Fig. 2b). Looking now at the case with the time constant $\tau = 0$, the second term in Eq. (1) simply describes a second reaction with the parameters R_s and C_s related to semicircle 3 in Fig. 2b. Allowing a finite τ (and ignoring C_s), the second term then describes a relaxation process from a resistance R_s at low frequencies to an increased resistance $R_s + \Delta R_s$ at high frequencies. The corresponding time constant discriminating ‘high’ and ‘low’ is just τ . That the spectra can be fitted by this equation shows that the measured data can indeed be described as ‘semicircles’.

The time development of the fitting parameters for the resistances when switching several times between cristo and curro pore growth is shown in Fig. 2a. Although the precise chemical meaning of these parameters is not yet clear, it is quite obvious that the resistances differ strongly for the cristo and curro pore growth regime. In particular, the changes in R_p are quite drastic (note the logarithmic scale for this resistance). From a nearly constant value in the curro pore growth phase it (surprisingly) increases by several orders of magnitude (cf. point *c* in Fig. 2a) within a few seconds when reducing the voltage to form cristo pores, and afterwards quickly reduces to stable values significantly smaller than in the curro phase. Examples of Nyquist plots in this phase of rapidly decreasing R_p are shown in Fig. 2c. For the subsequent growth of stable cristo pores only a monotonic decrease of R_s is found. Examples of Nyquist plots in this phase (cf. Fig. 2d) therefore have all the same shape and just shift to lower real parts as a function of increasing depth of the cristo pore layer. In the curro pore growth phase only minor changes are found in the impedance. An example of a typical Nyquist plot is shown in Fig. 2e.

With respect to the statements and claims made in the Section 1, the results not only demonstrate the power of the method, but the necessity for very fast data generation. More systematic experiments will be needed to unravel in detail the mechanisms behind the cristo \leftrightarrow curro switch-over, but some general points can be already made based on the data given.

These impedance data plus other experimental findings indicate that, due to the large aspect ratios of the pores, diffusion limitations of reaction products and educts from and to the pore tips are an essential part of curro pore growth. When growing curro pores at high current densities, therefore, a noticeably lower reactant concentration at the pore tips can be expected than for growing cristo pores at low current densities. This implies that right after switching from curro pores to cristo pores by reducing the applied voltage one can expect a much smaller reactant concentration at the pore tips than some seconds later in the stable phase of cristo pore growth. The drastic decrease of R_p (after the initial peak) may therefore indicate the now increasing concentrations of the active electrolyte components near the pore tips that is established as the new steady-state condition for the lower current density.

At first glance it may appear astonishing to find a decrease of R_s while a cristo pore layer is formed since ohmic losses should increase with the thickness l of the (cristo) porous layer. On the other hand, it is a well-known fact that cristo pores nucleate in a small density and afterwards ‘fill’ the available space by heavily branching. This branching leads to a rapid increase of the overall pore tip area A with time, which may well overcompensate the increase in layer thickness according to $R_s = \Delta/lA$. In steady state R_s stays nearly constant or increases slightly and R_p is constant as well, despite the undisputed fact that with increasing layer thickness ohmic and diffusional resistance effects must increase monotonically.

The experimental finding of nearly constant values for R_s and R_p during stable cristo pore growth thus can be seen as an important input concerning the formation mechanism for cristo pores. One might speculate that there exists an optimal current density j_{cy} for the dissolution at the cristo pore tips, which depends on the electrolyte parameter and the applied voltage, and which the pore maintains in a self-organized manner. At high voltages, i.e. forcing a higher current density through the interface, the cristo pores will branch, until j_{cy} is reached at the pore tips. With increasing layer thickness j_{cy} will decrease, duly compensated by further branching. According to this model, j_{cy} is directly related to the possibility of forming side pores, which within the framework of the current burst model of the authors [38–40] can be directly related to the time constants for passivation of $\langle 111 \rangle A$ and $\langle 111 \rangle B$ surfaces in InP, which brings us back to the original statement that the interplay of various time constants involved in the etching process determines what will happen. A more detailed discussion and a further quantitative analysis of the impedance data for various etching conditions will be presented elsewhere.

4 Use of combined back-side illumination impedance and voltage impedance during macro-pore etching in n-type Si

4.1 Voltage-current FFT impedance and interpretation of the data obtained Conventional UI impedance, while not new, has not previously been applied to

n-Si-macro(bsi) pore etching, because of the many special requirements mentioned above. A specific problem originates from the necessary current saturation condition, implying that small variations in the applied potential do not produce substantial responses in the current. In other words, there is a severe signal-to-noise problem.

With the optimized electrochemical processing system described before, it is now possible, as in the case of InP, to obtain meaningful UI impedance spectra during pore etching; some preliminary results have been reported in [25]. Two recent examples are shown in Fig. 3. The spectra are reproducible and the quality is quite good; it only remains to interpret the data in a meaningful way.

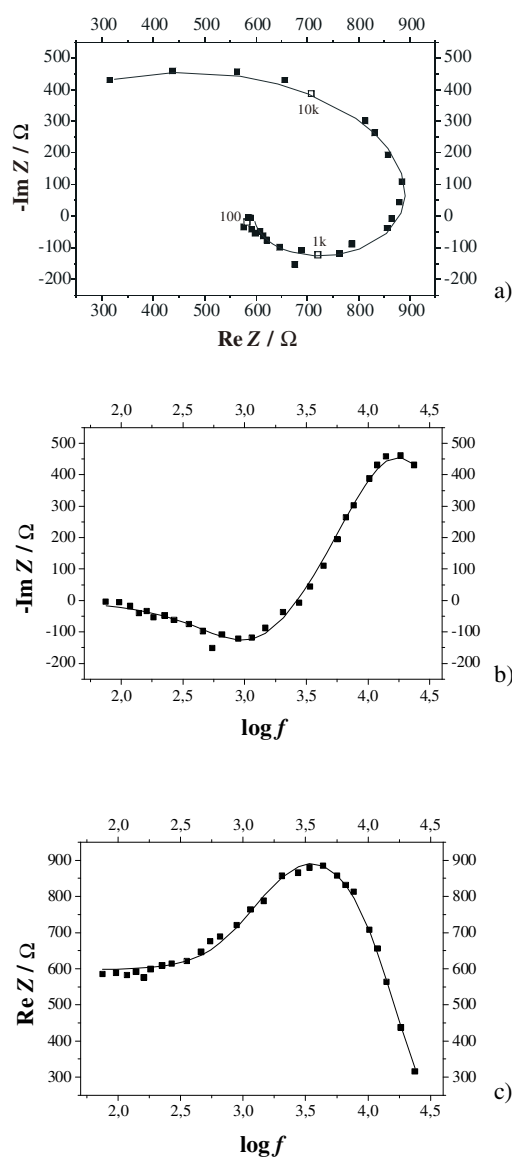


Figure 3 Typical UI spectra. a) Nyquist plot; the corresponding Bode plots for b) the imaginary and c) the real part of the impedance. Measured data (squares) and the fit employing Eq. (2) are shown.

From general impedance theory a number of interconnected semicircles should be expected in the Nyquist plot if diffusion of ions can be neglected in the investigated frequency regime [1]. In Fig. 3 two semicircles are visible. The most remarkable feature of the UI impedance is the negative or inductive semicircle at low frequencies. Spectra like these are known from many electrochemical processes: they may be caused quite generally from dissolution processes that proceed by more than one reaction if at least two reactions have sufficiently different time constants [1], or by the formation of some kind of blocking layers [41–43]. In Si, inductive loops have been reported by a number of groups, e.g. Searson and co-workers [44, 45] and Ozanam et al. [46], but under conditions where no pores

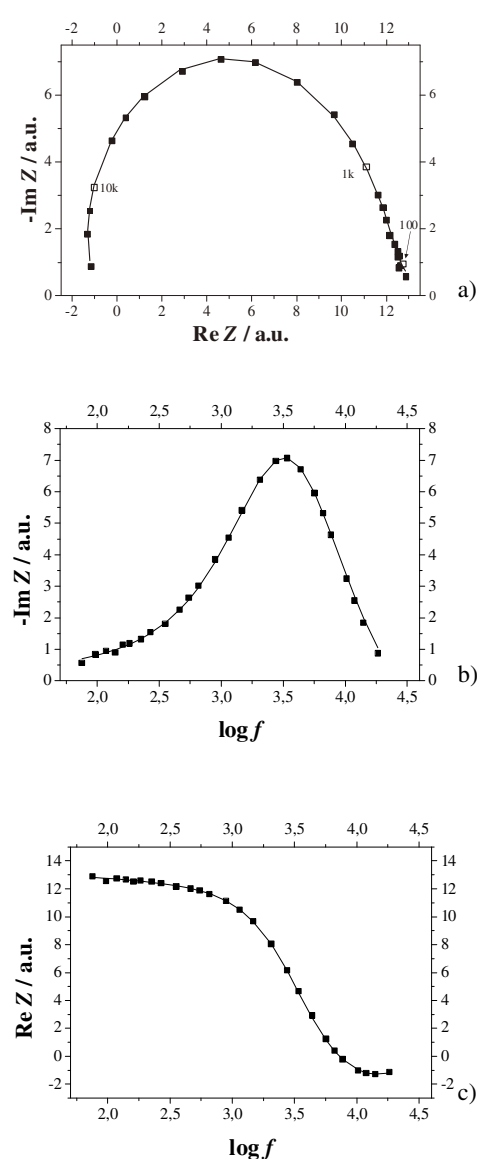


Figure 4 Typical bsi-PI spectra. a) Nyquist plot; the corresponding Bode plots for b) the imaginary and c) the real part of the impedance. Measured data (squares) and the fit employing Eq. (13) are shown.

are growing. Explanations given ranged from oxide layer formation [44] to increasing potential drops in the Helmholtz layer [45], to surface roughening [46]. The list is not complete but suffices to demonstrate that there is no directly obvious explanation for inductive semicircles. However, since *ex situ* UI impedance measurements, i.e. measurements done with rough or porous electrodes after the roughening or pore forming process, respectively, tend not to show inductive loops [47–51], it is reasonable to assume that the inductive loops observed in situ here are not primarily caused by the surface topology but reflect different time constants of the electrochemical reactions occurring during pore formation. This is further corroborated by the observation that just diffusion limitation does not usually produce inductive loops either [52, 53]. We will thus proceed by assuming that at least two processes with different time constants need to be considered to interpret the spectra obtained.

Since existing models for n-Si-macro(bsi, aqu) formation require two distinctly different reactions at the pore tip as detailed below (e.g. [2]), standard two-reaction impedance models for curves of this type have been tried. The two-reaction UI impedance model expressed by

$$Z(\omega) = R_s + \frac{1}{\left(\frac{i\omega\tau}{(R_p + \Delta R_p)(1 + i\omega\tau)} + \frac{1}{R_p(1 + i\omega\tau)} \right) + i\omega C_p} \quad (2)$$

and found in parts, for example, in [1], provided very good fits to the data and thus is used in what follows.

Note that Eq. (2) is a simpler version of Eq. (1), which encodes three distinguishable processes; in addition it employs a simple series resistance term R_s . Following the standard interpretation of such a model, R_s describes the ohmic losses, C_p describes the capacitance of the interface, and R_p the chemical transfer resistance of the chemical dissolution process. The chemical dissolution splits into two processes with different reaction rates characterized by the relaxation time τ of the slow process and the time constant $R_p C_p$ of the fast process. The difference ΔR_p describes the increase in the chemical transfer resistance at higher frequencies.

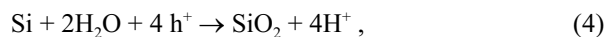
Equation (2) has proven perfectly adequate for fitting several thousand spectra obtained under quite different conditions very well, lending credibility to the assumptions involved. If we take Eq. (2) thus as not only a mathematically adequate description of certain curves, but also as a sufficiently good description of the two electrochemical processes occurring at the interface, we can go one step further and derive the effective valence n of the dissolution process, i.e. the externally measured average of the valence of the direct dissolution process (typically around 2) and the valence of the oxide formation process (always 4), from the UI impedance data. It is well known that n is one of the most important parameters for successful pore etching; monitoring n in situ is thus highly desirable.

First, we use established process knowledge and identify the two processes in question as direct dissolution of Si and oxidation of Si. Direct dissolution proceeds according to the sum reaction equation



The valence n_d of the direct dissolution process, i.e. the number of holes needed to remove one atom of Si, is $n_d = 2$ in the case of Eq. (3). Upon closer inspection of direct dissolution processes it might also be somewhat smaller or larger than 2 [2], if more or less than two electrons are injected on average; but for the sake of simplicity we take it to be 2 for what follows.

Oxidation (followed by purely chemical dissolution of the oxide in order to dissolve Si) proceeds according to the sum reaction equation



the valence of oxidation alone thus is always $n_{ox} = 4$. It has been known for a long time that the valence encountered during n-Si-macro(bsi, aqu) pore etching is around 3 and that the quality of the pore etching is critically dependent on achieving conditions that provide a valence of 2.7 on average [2]. Discounting the possible but highly unlikely occurrence of direct dissolution with a valence $n_d \gg 2$ under these conditions, this is obviously only possible if both dissolution reactions occur simultaneously in some mix for n-Si-macro(bsi, aqu) pore etching.

The effective dissolution valence during pore etching in terms of the electrochemical reactions thus can be generally expressed as

$$n = 2\alpha + 4(1 - \alpha) , \quad (5)$$

with α being the fraction of direct dissolution with valence 2 and $1 - \alpha$ being the fraction of oxidation with valence 4. Impedance data, however, can only give the respective fractions β of the slow and fast process; relative to this distinction the effective valence is written

$$n = n_1\beta + (1 - \beta)n_2 , \quad (6)$$

where β is the fraction of the fast process with valence n_1 ; the valence n_2 then belongs to the slow process. The slow and the fast process are not necessarily uniquely coupled to one (electro)chemical process each; in principle they could also be mixtures of the divalent and tetravalent process with different mixing ratios. To give an example for this, consider dissolution by oxidation alone. It consists of (anodic) oxide formation and (purely chemical) oxide dissolution – the total or sum process is a mixture of two individual processes having usually quite different time constants. While there is no compelling reason to consider mixtures of divalent and tetravalent processes in this connection, it cannot yet be ruled out either.

While it is tempting to identify the slow process as oxidation only (i.e. $n_1 = 2$, $n_2 = 4$, $\beta = \alpha$), there is no theoretical justification for this assumption at this point. We

will therefore first derive an equation for the valence n in terms of β . In a second step it will be shown that the measured time dependence of n only allows the case $\beta \approx \alpha$, proving that oxidation does indeed dominate the slow process.

If we now consider the (small) voltage drop U at the interface caused by the slow Si dissolving process (i.e. $\omega \rightarrow 0$ Hz), it is given by

$$U_{\text{slow}} = I_{\text{slow}} R_p = [n_1 \beta + (1 - \beta) n_2] N R_p, \quad (7)$$

where I_{slow} is the (small) current flowing across the tip interface and N is a proportionality constant (in fact N is the number of Si atoms dissolved per second times the elementary charge). The resistance R_p is the correct value in this case as can be easily seen from Eq. (4). Note that only the current flowing through the resistors R_p and ΔR_p dissolve Si, while the current flowing through the serial resistance R_s does not.

Looking at the high-frequency end (i.e. $\omega \tau \gg 1$), only the fast process can carry current, and we obtain

$$U_{\text{fast}} = I_{\text{fast}} (R_p + \Delta R_p) = n_1 \beta N (R_p + \Delta R_p), \quad (8)$$

with I_{fast} being the current for the fast process only. For potentiostatic experiments we have $U_{\text{slow}} = U_{\text{fast}} = U_{\text{slow/fast}}$; by combining Eqs. (7) and (8) we thus obtain

$$F := \frac{\Delta R_p}{R_p + \Delta R_p} = \frac{n_2 (1 - \beta)}{n_1 \beta + n_2 (1 - \beta)}. \quad (9)$$

Solving Eq. (9) for β and insertion into Eq. (6) allows one to extract numbers for n from measures of the impedance spectra, if values for the valences n_1 and n_2 for the fast and slow process, respectively, are assumed. There are essentially three basic scenarios for this:

1. The slow process is (mostly) 'oxidation' (meaning oxide formation and dissolution in this context); in this case $\beta = \alpha$, $n_1 = 2$, $n_2 = 4$.

2. The slow process is (mostly) direct dissolution; in this case $\beta = 1 - \alpha$, $n_1 = 4$, $n_2 = 2$.

3. Arbitrary mixtures obtain; in this case α cannot be determined from measuring β without additional input.

A decision about which scenario is the most likely can only be made with independent information about the pore dissolution process. Fortunately, it is known that the effective valence $n(t)$ can only decrease with time during pore etching, because with increasing time the potential at the pore tip can only decrease and the leakage currents through pore walls can only increase, too; both effects will emphasize divalent dissolution (e.g. [2, 54]). Only scenario 1 produces a decreasing $n(t)$; scenario 2 would produce an (mirror symmetric) increasing $n(t)$; scenario 3 produces anything in between scenarios 1 and 2. This experimental fact justifies choosing $n_1 = 2$, $n_2 = 4$; at least as a good approximation. For this case Eq. (9) gives

$$\beta = \frac{2F - 2}{F - 2}, \quad (10a)$$

and the final equation for extracting the effective valence n from the impedance data then is

$$n = 2\beta + 4(1 - \beta) = \frac{4}{2 - F} = \frac{4}{2 - [\Delta R_p / (R_p + \Delta R_p)]}. \quad (10b)$$

Questioning this interpretation would be an academically valid but moot point with respect to experimental reality. Experimental results from more than 20 etching experiments performed while monitoring $n(t)$ as given by Eq. (10) consistently showed that good results in the sense of uniform deep pores without a destroyed surface are only obtained if the $n(t)$ curve stays around a value of 2.8, which is exactly what the effective valence is supposed to do according to detailed studies of Lehmann [2]. Accepting that, the importance of Eq. (10) for pore etching is obvious and large: it allows for an in situ assessment of the dissolution valence, arguably the most important parameter for uniform pore growth.

Of course, besides yielding $n(t)$, the values of the three resistors, the capacitance C_p , and the time constant τ contained in Eq. (2) can also be plotted as a function of time; Figs. 7 and 8 show examples. Besides the interpretation of the resistances already given in the discussion above, no further meaning will be attached to these quantities at present. However, the impedance spectra yield some more information about the system if explored in the light of the knowledge already gained. In particular, the slow process has now been identified as Si oxidation; the time constant τ thus assigns a number to this process. The complete process of dissolving Si by oxidation involves anodic oxidations and purely chemical dissolution; the question now is which of these two processes determines τ . Anodic oxidation experiments (e.g. [2, 3]) prove that anodic oxide formation is quite fast, leaving oxide dissolution as the rate-determining step. Accepting this, the corollary is that the pore tip surface is covered with a thin oxide layer most of time, at least for optimal macropore growth.

This is an important statement with many repercussions. First, it implies that the voltage drop occurs mainly in the oxide and not in the Si. In other words, the width of the SCR calculated from the standard equation including only the doping concentration of the Si drastically overestimates the space charge region around the pore tip, just small 'remnants' from whatever small amount of the potential still drops in the Si. Second, the capacitive behavior of an oxide-covered tip would be quite different from that of a tip without oxide. Third, if oxide coverage is responsible for the sluggish response to high-voltage modulation frequencies, it must be expected that the response to high bsi modulation intensities is sluggish, too. More implications will be discussed in the context of the second set of data obtained by bsi-PI.

4.2 Back-side illumination FFT impedance and interpretation of the data obtained Since this is the first time that bsi FFT PI measurements have been per-

formed, a short description of this mode will be given first. Figure 5 shows the typical set-up for etching n-Si-macro(aqu, bsi) pores and defines the parameters needed for what follows. In essence, the present understanding (which needs to be augmented later on) is as follows. Electron–hole pairs are generated by the back-side illumination in a comparatively thin layer right behind the back-side surface of the sample. For the particular geometry given and under ‘normal’ pore etching conditions, it is a good approximation to assume that all minority carriers (i.e. holes, the only carrier type that is of importance here) are generated right at $z = d_w$, and that no recombination at the back-side surface occurs (i.e. the back-side surface recombination velocity $S_b = 0$ cm/s). This can be expressed as an illumination-induced current density $j_b(z = d_w)$ at the back side that is directly proportional to the illumination intensity P at the back side.

The photo-generated holes diffuse in the sample; some recombine in the volume of the sample (a process described by the minority lifetime τ or the diffusion length $L = (D\tau)^{1/2}$, where D is the diffusion coefficient of the minority carriers), some reach the pore tips (with a total current density j_p) and are consumed immediately. For constant illumination intensity and within the assumptions made, j_p is exclusively a function of the injected photo-current j_b , the diffusion length L , and the remaining bulk thickness d_B of the Si as defined in Fig. 5.

As postulated in [55], the basic assumption is that all the current j_p at $z = d_p$ is consumed at the pore tips and leads to pore growth in the z -direction only. In mathematical terms this translates into the boundary condition that the recombination velocity S_p at a plane at depth z is given by $S_p(z = d_p) = \infty$, or, in order to avoid problems with infinities later, $1/S_p(z = d_p) = 0$.

However, as discussed to some extent in [15, 25, 26], the experiments prove that this is actually not a very good boundary condition, and this means that the basic assumption of the macropore etching model of Lehmann and Föll first given in [55] is not sufficient to explain macropore formation and growth. Since one of the authors of the present paper (H. F.) conceived this model, this statement is important in this context and shall be enlarged upon later.

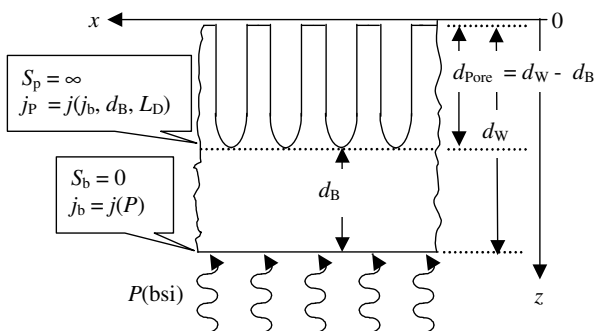


Figure 5 Parameter definition for etching n-Si-macro(aqu, bsi).

Under the assumptions given, the current j_p available at pore tips at position z in the sample can be calculated from the diffusion equation for the carrier density $n_h(x, y, z, t)$, including generation and recombination terms, in the form

$$D \Delta n_h - \frac{n_h - n_{h,0}}{\tau} + F(1 - R) e^{-\alpha z} = \frac{\partial n_h}{\partial t}, \quad (11)$$

where Δ is the delta operator in this case, D the diffusion coefficient of the minority carriers (holes), $n_{h,0}$ the carrier density at equilibrium, τ the minority carrier lifetime, R the reflectivity, $F(1 - R) = P$ the photon intensity, and α the light penetration depth.

The static one-dimensional solution (light intensity P constant in time and negligible penetration depth) for $j_p(d_B, L)$ can be found in semiconductor textbooks (e.g. [56]); it plays an important role in the electrochemical characterization of single-crystalline or multicrystalline Si wafers with the so-called ‘ELYMAT’ technique [57–59]. The time-dependent one-dimensional solution $j_p(\omega, d_B, L)$ for light intensities sinusoidally modulated with a circle frequency ω and amplitude A is easily derived in this case, too. The measured response contains a current component $j_{sem}(\omega, d_B, L)$ from the semiconductor only, and the semiconductor part Z_{sem} of the bsi-PI impedance can be defined as the ratio $dj_{sem}(\omega, d_B, L)/dP(\omega)$, again assuming that the penetration depth of the light is much smaller than the remaining wafer thickness d_B and that the surface recombination at the illuminated back side of the wafer is zero. One obtains

$$Z_{sem}(\omega, d_B, L) = \frac{dj_{sem}(\omega, d_B, L)}{dP(\omega)} \propto \frac{1}{\cosh \left[d_B \sqrt{(1/L^2) + (i\omega/D)} \right]}. \quad (12)$$

The total impedance of the system has also to take into account the transfer of the holes (and possibly reactions involving electron injection at the interface), as well as the transport of the current through the electrolyte. However, injection of electrons always needs to be triggered by at least one hole; this process therefore would only change the proportionality constant implicitly contained in Eq. (12). Current transport through the electrolyte can be neglected, since by definition the process takes place under saturation conditions. In other words, the electrolyte part of the system could ‘handle’ far larger currents and thus adds at most some (trivial) small serial resistances.

The impedance defined by Eq. (12) has been matched to measured FFT PI spectra as shown in Fig. 4; see also [15, 25, 26]. While the match was relatively good, it was not yet perfect, in particular for high and low frequencies; this is shown in greater detail in Fig. 6. Nevertheless, from the match at any ‘pixel’ in time it was possible to extract the pore depth $d_p(t) = d_w - d_B(t)$ as a function of time with some accuracy. In preliminary short papers [15, 25, 26]

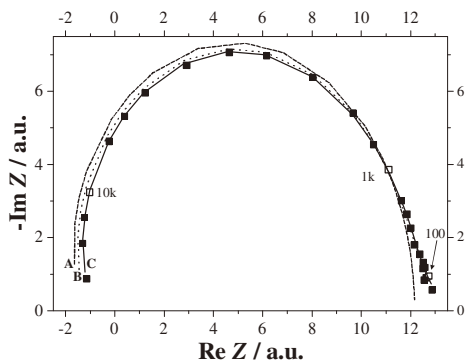


Figure 6 Improving the fit to measured in situ bsi-PI spectra (black squares). Curve A results from Eq. (12) only. Curve B results from Eq. (13) without the diffusive term, and curve C is based on the complete Eq. (13). Numbers indicate the frequency in Hz. The impedance measurements have been conducted at intervals of 1 s in a frequency range between 10 Hz and 40 kHz, containing 27 frequencies as indicated.

some attempts were also made to extract the diffusion length $L(t)$. This, however, was only possible if an unspecified Warburg-type impedance was added to Eq. (12), but, even then, a pronounced (and unphysical) time dependence of $L(t)$ was found. Omitting details, an analysis of possible shortcomings of Eq. (12) showed unambiguously that the main problem lies in the assumption that all holes reaching the space charge region will be focused immediately on a pore tip, i.e. the assumption that $1/S_p(z = d_p) = 0$.

It emerged that this boundary condition needs to be modified in two ways if physical reality is to emerge. First, there is a finite probability that holes reaching points between pores will ‘escape’ and end up not on pore tips, but recombine somewhere or diffuse between the pores and cause (leakage) currents through the pore walls. In mathematical terms the recombination velocity SP of the fictitious plane at $z = d_p$ then becomes a (periodical) function of position (x, y) , with a value that is smaller by some $\Delta(1/S_b)$ between pores as compared to the value at pore tips.

Second, considering the finding from the UI impedance measurements that the tip is covered with oxide most of the time, the implications are that the holes, trapped in whatever small space charge region still exists around the pore tips, cannot be processed most of the time and have to keep diffusing in the SCR confined space around the pore tips. This means that holes arriving at the general pore tip area may have to ‘wait’ for a while, before they can dissolve Si at the pore tip and this effect, if present, would be felt more at higher frequencies than under more static conditions. In mathematical terms it means that an additional diffusion term for holes, similar to a Warburg impedance for ions, needs to be added to Eq. (12).

Taking account of these two modifications poses a formidable mathematical problem. The solution as shown in Eq. (13) was found by a two-tiered approach. First, the diffusion equation was solved for the periodic boundary conditions imposed by the first statement above, adding the

term in the second bracket of Eq. (13) that contains the difference $\Delta(1/S_b)$ introduced above (in the form of $\Delta(D/S_b)$ because surface recombination velocities always occur in the form of D/S). While this allowed a much better fit of the measured data, in particular for low frequencies, a perfect fit was only obtained by adding the diffusive term in the first bracket that is dominated by $A_2(i\omega)^{1/2}$ (it is simply proportional to Z_{sem} for $A_2 \rightarrow 0$):

$$Z_{complete}(\omega, d_b, L, \Delta S_b) = A_1 \left[Z_{sem}(\omega, d_b, L) + \frac{A_0}{1/Z_{sem}(\omega, d_b, L) + A_2 \sqrt{i\omega}} \right] \times \left[\frac{1/\sqrt{1/L^2 + i\omega/D}}{1/\sqrt{1/L^2 + i\omega/D + \Delta(D/S_b)}} \right]. \quad (13)$$

The diffusion term could not be directly obtained from solving proper three-dimensional equations, but was chosen as an approximation in linear order of the three-dimensional boundary condition induced by the pore tips, and it gave the best fit to thousands of spectra. Figure 6, showing the Nyquist plot of Fig. 4, fitted by Eq. (12), Eq. (13) without the diffusive term, and the full Eq. (13), demonstrates this. As can be seen, the fit with the full Eq. (13) is excellent – not only for this example but also for the thousands of spectra obtained in the experiments performed so far.

As before, the validity of Eq. (13) with respect to describing physical reality can be doubted to some extent, but in contrast to, for example, Eq. (10), a large part of Eq. (13) is beyond doubt, because it describes exactly the problem posed by the diffusion equation, which in turn describes exactly the physical reality within the (trivial) assumptions made.

From an experimental point of view, Eq. (4.12) allows one to extract in situ a number of parameters that are not only helpful but have proved to be correct whenever experimentally checked. The following section addresses this point by giving two examples.

4.3 Results of pore etching experiments employing bsi-PI and UI FFT impedance spectroscopy

All experiments were run under the following general conditions:

- Specimen: n-type Si, doping 1–10 Ω cm, {100} oriented, implanted n^+ back-side contact, mostly lithographically structured front side with a hexagonal or square array, lattice constant = 3.9 μ m. Typically the sample size was 1 cm^2 .

- ET&TE etching system ELYPOR 02 with full PC control of an LED array for illumination of the back side to ensure the desired etching current (and of all other parameters). FFT impedance spectrometer: ET&TE system for fully automated in situ impedance data acquisition and analysis for UI and PI.

- Etching conditions differed somewhat. In Fig. 7 a standard aqueous electrolyte with an HF concentration of

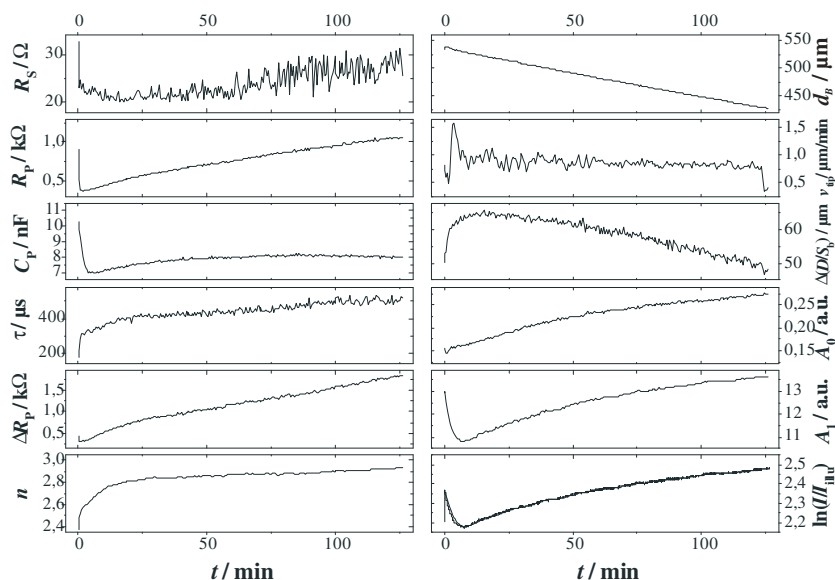


Figure 7 Very stable etching conditions with rather constant valence using ‘standard’ aqueous electrolyte at 5 wt% for applied voltage $U(t)$ of 0.4 V and etching current $I_{ex}(t)$ from 20 mA/cm² to 18 mA/cm² was obtained, using a peristaltic pump with a pump rate of 100 rpm. Left side: Results of UI impedance as described by Eqs. (2) and (10). Right side: PI as described by Eq. (13) and, at the bottom, the logarithm of the ratio between dc etching current and dc illumination intensity. Pores obtained look ‘perfect’ and are not shown here. See text for details.

5 wt% was used, whereas Fig. 8 shows results obtained with the same electrolyte as in Fig. 6 to which 0.85 g/l of carboxymethylcellulose salt (CMC) has been added.

In any etching experiment, the duration of a time ‘pixel’ was defined to be 1 s. A complete bsi-PI spectrum was taken within one time pixel (measurement time = 0.6 s), followed by a pixel of ‘rest’ and an UI spectrum in the third pixel, again followed by a ‘rest’ pixel. Two complete spectra thus take 4 s altogether; in a typical experiment running for 5 h, 4500 spectra resulted. The voltage perturbation had a peak-to-peak amplitude of up to 50 mV for the sum of the 30 applied frequencies and the illumination intensity had a peak-to-peak amplitude of up to 80 μA corresponding to 0.01% of the total illumination intensity. Parameter extraction from the spectra obtained was done in real time. The resulting quantities are plotted and dis-

played; Figs. 7 and 8 give examples. In both Figs. the left-hand column displays the data from the UI measurements, the right hand column the data from the PI measurements plus a consistency check diagram. In both cases rather perfect macropores with depths around 250 μm were obtained; pertaining figures. have been shown in [15, 25, 26], and, for the sake of brevity, shall not be reproduced here.

In the foregoing discussion much has been said as to the meaning or the interpretation of some of the parameters involved. Far more could be said here, but we will forego a detailed discussion and only point out a few major points. The etched area was defined by pressing the Si sample directly on an O-ring. The illuminated area is defined by the size of the LED array, which is in direct contact with the back side of the wafer. When the pores grow into the depth, additional holes from the periphery will diffuse to the pore

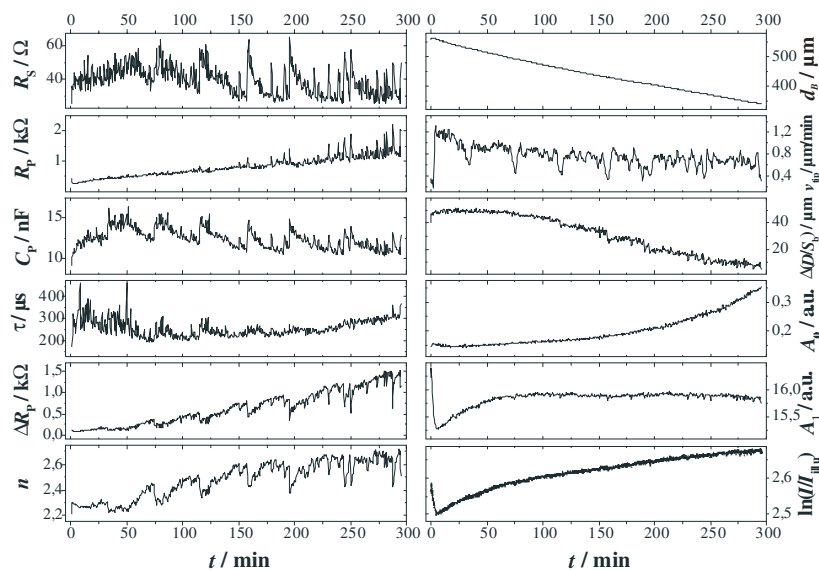


Figure 8 Etching conditions where pore growth repeatedly almost stops for short time periods. Aqueous electrolyte with an HF concentration of 5 wt% with 0.85 g/l of carboxymethylcellulose salt (CMC) was used. The voltage of 0.7 V and etching current $I_{ex}(t)$ decreasing from 15 mA/cm² to 10 mA/cm² was applied using a peristaltic pump with a pump rate of 100 rpm. Left side: Results of UI impedance as described by Eqs. (2) and (10). Right side: Results of PI as described by Eq. (13) and the logarithm of the ratio between dc etching current and dc illumination intensity. See text for details.

wall at the edge of the etch area leading to an under etching or lateral pore growth in the O-ring area and thus to an increased effective etching area. This geometrical increase is reflected in the parameter A_1 , which essentially represents the gross etching area (up to a scaling factor taking into account, for example, the reflectivity at the back side of the wafer). It can be seen that after a nucleation phase of roughly 15 min, A_1 is increasing monotonically. If this effect is ignored, a calculation of the current density necessary to ensure a constant pore diameter will be somewhat faulty and the pore diameters will decrease as a function of time. In addition, the problem with a non-constant diffusion length L , discussed in preliminary publications as stated above, can also be explained to some extent by this effect since only in the beginning of an experiment does a flat etching area exist, which can be perfectly described by a one-dimensional diffusion model. Luckily, the diffusion length is the only fitting parameter which is significantly affected by the increase of the effective etch area. By setting the diffusion length L to the value obtained by fitting at the beginning of the experiment when the etch area is still flat, all remaining fitting parameters give reasonable results for the full experiment. In particular, the d_B curve shows a nearly perfect linear decrease as a function of time. This describes a linear pore growth into the wafer with a monotonically decreasing layer of bulk Si with thickness d_B . The negative derivative of this curve describes the velocity v_{tip} of pore growth at the tips, which, despite some measurement noise, is remarkably constant and only shows an expected slight decay for longer etching times due to the diffusion limitation-induced reduction of the HF concentration at the pore tips. These results are in good agreement with the ex situ SEM results on this sample. As stated earlier the valence extracted for this nearly 'perfect' etching experiment is indeed rather constant and found to be about 2.8. Note that this number is derived without using prior knowledge, i.e. it has never been directly or indirectly used in the calculations.

We will now turn to the example shown in Fig. 8 that provides rather different impedance data, but still, according to the SEM results, very good pore quality. In this case a special 'viscose' electrolyte as specified in the figure caption has been used that was optimized because it improves certain features of n-Si-macro(aqu, bsi) pore etching like pore wall roughness [54] akin to the case of TiO₂ nanotube growth [60]. The example was chosen in such a way that pore parameters like growth speed and final depth are similar to those shown in Fig. 8. It is obvious that, especially, the UI IS data shown on the left in Fig. 8 are far more dynamical than the corresponding ones in Fig. 7, showing several spikes in nearly all parameters. These spikes are not obvious in the direct illumination impedance data. However, while the d_B curve looks rather smooth, its negative derivative does show a very interesting feature. Each time the UI data show a spike, the growth velocity v_{tip} at the pore tips decreases markedly. Note that the dips in the v_{tip} curves cannot be fitting artifacts since the illumi-

nation impedance is sensitive to the actual thickness of the remaining bulk Si. If the dip in the pore growth speed were an artifact, it necessarily needs to be compensated by corresponding regimes of increased pore growth – which are not found. A further validity check for the illumination impedance is possible from the data for A_1 . In comparison to the experiment shown in Fig. 7, the experiment in Fig. 8 took much longer (by a factor of about 3), and after about 100 min A_1 stays remarkably constant. This, as outlined above, indicates that the under etching slows down and stops for a certain length of side pores, which is consistent with the pore morphologies seen in SEM images. As soon as the effective etching area stays constant, the diffusion of holes through the bulk Si only depends on the monotonically decreasing thickness of the Si layer. In this case an exponential increase of the ratio between etch current I and illumination intensity I_{illu} should be expected, and a linear increase of $\ln(I/I_{illu})$ respectively. Exactly this behavior is found for the ratio of the corresponding dc parameters. The stronger increase in the first period of the experiment just reflects the additional increase in the area.

Since no spikes are visible in the dc etching current, the dc illumination intensity, or the SEM images of the pore diameters, the observations that substantial variations of the pore lengths between nominally identical experiments have been found could not be understood without the impedance data. In contrast, knowing in situ the number of spikes, i.e. the number of phases of decreased pore growth velocity, the desired pore length can be obtained by a corresponding increase of the etching time.

We chose this example rather than one showing problems with uniform pore growth occurring after some etching time (suffice it to say that this is noticeable in the impedance data) to demonstrate two major points connected to macropore growth that are not always appreciated in the literature.

1. Macropore growth is a dynamic nonlinear process with various degrees of self-organization. Mainly due to diffusion phenomena (holes within the Si wafer and ions through the length of the pores), the etching conditions continuously change in a strongly nonlinear way, reflected in the change of nearly all fitting parameters in Figs. 7 and 8. In order to ensure, for example, a constant porosity or a constant pore diameter, respectively, much effort is needed for ex situ optimization of etching parameters. In many cases, e.g. if the current inside individual pores actually oscillates in a self-organized manner due to variants of the mechanism described in [40], no efficient ex situ control is possible at all.

2. It is one thing to obtain in situ data about the processes occurring during pore etching, but it is a different thing to draw conclusions from these data. Figure 8 demonstrates that neither the quality of the etching process can be easily deduced from in situ data, nor the best control algorithm, i.e. which external parameter should be changed in what way to keep the process at optimum conditions.

Notwithstanding these critical remarks, it goes without saying that the data obtained so far have proved to be quite useful in etching n-Si-macro(aqu., bsi) pores, and further work will no doubt enlarge the database, helping to move pore etching from an art into the realm of applications based on reproducible (and hopefully automated) production.

5 Front-side illumination FFT impedance spectroscopy

5.1 Some peculiarities of front-side illumination FFT impedance spectroscopy

Pore etching under front-side illumination is not a commonly employed etching mode for the simple reason that the absorption depth of the light is typically much shorter than the (macro)pore depth aimed for. However, n-Si-macro(fsi, aqu/org) pores have been obtained and several peculiar features have been observed that have never been fully explained. In the case of pore etching in III–V semiconductors or in SiC, ultraviolet (UV) fsi has on occasion found to be useful for a better nucleation of macro- or mesopores [61]. FFT impedance measurements under fsi conditions thus might be of some value for pore etching issues, but this needs to be shown in future work. This has been done before; for example, the linear response of the photo-potential of intensity modulated local laser illumination has been investigated [71], and direct PI analysis has been used to study electrolyte–insulator–semiconductor structures as well [24].

If fsi impedance spectroscopy is used for direct semiconductors, where it can be safely assumed that photo-induced carrier generation takes place in a very thin layer right behind the surface (i.e. in the space charge region) [17–21], no information about the bulk can be obtained but ‘only’ data about carrier transfer across the interface. Looking at the far more complicated case where carriers are also generated, diffuse, and recombine deep in the bulk (i.e. looking essentially at Si electrodes), will allow one to characterize (indirect) semiconductor materials with respect to bulk parameters that are of importance, e.g. for solar cell production.

In this case the short-circuit current j_{SC} is a function of several parameters. The most important ones are as follows.

The reflectivity R of the surface. Light that is reflected obviously cannot contribute to j_{SC} .

The penetration depth α of the light. Minority carriers generated deep in the bulk have a smaller probability to reach to the junction, producing current.

The minority carrier lifetime τ_{min} , or the directly related diffusion length $L = (D\tau_{min})^{1/2}$. D is the diffusion coefficient of the minority carriers, which is related to the commonly used mobility μ by the Einstein relation $D = kT\mu/e$ (where e is the elementary charge and k the Boltzmann constant). The diffusion coefficient D of the minority carriers, coupled to (local) doping and all kinds of defects (and of course the temperature), is therefore also a quantity of considerable interest that needs to be determined.

The recombination velocity S_b at the back side of the specimen. Photo-generated minorities lost at the back side cannot contribute to j_{SC} , so the back-side conditions must be considered as long as the sample thickness d_w (a ‘trivial’ parameter) is not much larger than the diffusion length L .

The series resistance R_{ser} . While the series resistance is not very important for j_{SC} , it is still of major interest for the solar cell as a whole. It is tied to some extent to the conductivity σ and thus the doping concentration n_{dop} of the sample and to the nature of the front-side contacts (the ‘grid’ on regular solar cells).

Obviously, under semiconductor–electrolyte junction conditions that emulate short-circuit or reverse conditions of an all-solid-state solar cell, no information about the junction itself can be obtained. That is not a big problem in the realm of Si solar cells, however, because as soon as solar cell efficiencies are $>10\%$, the overriding interest is actually not so much on the junction side, but on reflectivity, back-side conditions, and in particular series resistances.

From impedance spectra obtained in the fsi-PI mode all the quantities enumerated above can be extracted – in principle. In Section 5.2 we show that it can also be done in reality, but only after a certain complication that will be addressed in the remainder of this section.

As in the case of bsi-PI impedance, the total impedance of the system is given by the impedance of the illuminated semiconductor (i.e. the behavior of the minorities between generation and disappearance by recombination) times the impedance Z_R of the rest of the system. As in the bsi-PI mode, Z_R should be negligible, but was included anyway in first data evaluations. However, no combination of the known Z_S (as shown in Eq. (14)) and reasonable Z_R values could match the measured impedance spectra – neither for semiconductor–electrolyte junctions nor for regular solar cells (i.e. semiconductor–semiconductor junctions). The basic problem was that fsi-PI spectra always showed resonant behavior that could not have been caused by Z_S and not by any Z_R terms that could reasonably model whatever was expected to happen outside the semiconductor.

The explanation for this is simple. The resonance is caused by the control loop inherent in any electrochemical experiment employing a reference electrode (and possibly a second reference electrode, too). The control loop consists of the potentiostat or galvanostat and the sample; the properties of this control loop, in particular the time constant τ_{loop} expressed as a resonance frequency $\omega_0 = 2\pi/\tau_{loop}$, are determined by both ingredients (and the geometry of the sample, the nature and position of the reference electrode, etc.). As long as the frequencies used for modulating an input quantity are far below the resonance frequency ω_0 of this control loop, it will not be felt; and this is always the case in conventional UI impedance and in bsi-PI. Using fsi-PI, however, the control loop cannot be neglected any more; it becomes part of the system to be characterized. Moreover, since the sample is part of the control loop, it is

not possible to just determine the frequency characteristics of the hardware with the aim of separating it from the data. There are several reasons why the hardware cannot be neglected for this. First, even with optimized hardware, it is difficult to impossible to achieve control loops with resonance frequencies in excess of some 100 kHz because of electronic limitations and stability concerns. Second, since under fsi conditions carriers are generated close to the collecting interface, it takes very short time for them to reach the interface, i.e. the current and therefore the impedance can follow large modulation frequencies quite easily. In other words, the specimen time constant of interest is given by $\tau = d_i^2/D$, where d_i is the (average) distance of travel for a carrier. In the case of bsi-PI, d_i is of the order of 100 μm ; for the fsi-PI mode, it is more like 1–5 μm . The limiting frequencies thus are easily different by a factor of 10^2 – 10^4 .

Cutting a long story short, just one case for fsi-PI spectroscopy shall be quantified at present, the case of a ‘standard’ high-efficiency ($\eta > 14\%$) p-bulk Si solar cell, having an antireflection layer, a p–n junction, a grid contact on the front side, and a back-side contact (always with a back surface field). In this case a fully quantitative analysis is possible. The p–n junction is assumed to be ‘perfect’ in the sense that the boundary condition for the differential equation controlling carrier transport is $S_s = S(x=0) = \infty$, i.e. all minorities reaching the space charge region of the junction at $x=0$ are swept out as current. The following equation then describes the theoretical fsi-PI in a sufficiently large illuminated pixel of a large solar cell with full precision:

$$Z_{\text{fsi}} = Z_{\text{Si}} Z_{\text{RC}} Z_{\text{Res}}, \quad (14)$$

where

$$Z_{\text{Si}}(\tau, D, S_B, R, \alpha, d_w, \omega) = qF(1-R) \frac{1}{1-(G/\alpha)^2} \times \frac{(G/\alpha)(1-S_B/D\alpha) - \tanh(d_w G)[(G/\alpha)^2 - S_B/D\alpha]}{(G/\alpha) - \tanh(d_w G)(S_B/D\alpha)} \quad (14a)$$

and

$$G = \sqrt{\frac{1}{L^2} + \frac{i\omega}{D}}, \quad (14b)$$

where τ is the lifetime of minority carriers; qF is the intensity of illumination (expressed in photo-generated charge); R is the reflectivity; α is the penetration depth of the light; S_B is the surface recombination velocity at the back side of wafer or solar cell; D is the diffusion coefficient of the minorities; and d_w is the wafer thickness. The two other terms in Eq. (14) are given by

$$Z_{\text{RC}} = \frac{1}{1 + i\omega R_{\text{ser}} C}, \quad (15)$$

where R_{ser} is the serial resistance from the illuminated spot/area to the reference electrode and C the capacitance of the illuminated spot/area. This term simply recognizes that the system has some resistances and capacitances, stemming mostly from the series resistance of the Si and the capacitance of the space charge layer that is not contained in Eq. (14).

The impedance due to the resonant loop of the complete control circuit can be described with sufficient accuracy by a simple and strongly damped resonant process via

$$Z_{\text{Res}} = \frac{1}{1 - (\omega/\omega_0)^2 + iK_F \omega}, \quad (16)$$

where ω_0 is the resonance frequency and K_F a damping constant.

The three terms together describe completely the behavior of minorities by considering the impedance of the Si itself, the impedance of the $R_{\text{ser}}C$ time constant that is always present, and finally the resonant behavior of the total system resulting from the feedback loop, characterized by a resonance frequency ω_0 and a damping constant K_F .

The total impedance for the case of a standard Si solar cell thus is a function of 11 variables:

$$Z_{\text{fsi}} = Z_{\text{fsi}}(\tau, D, S_B, R, \alpha, d_w, \omega, R_{\text{ser}}, C, \omega_0, K_F),$$

one of which is trivial (thickness d_w) and two of which are not of much interest (resonance frequency ω_0 and damping constant K_F). All one has to do now is to extract the 8 parameters of interest by matching measured fsi-PI spectra to Eq. (14). While this may appear hopeless, it is actually not too difficult, as shown in the next section.

5.2 Mapping properties of standard Si solar cells by fsi-PI spectroscopy All that needs to be done in principle is to take a solar cell, short-circuit it to a phase sensitive (ac) ampere meter, and to scan a modulated laser beam across it while measuring amplitude and phase of the induced current at any pixel (x, y) at sufficiently many frequencies. Since the system does not change in time, FFT techniques are not needed in order to avoid drift but only in order to reduce the measurement time. The results shown here have been obtained by a sequential technique since the FFT technique has not yet been added to the basic so-called ‘CELLO’ technique [62, 63] employed in this case (see below).

Doing things ‘in principle’ is not good enough in this case, however. The electrical behavior of solar cells with large efficiencies is influenced to a considerable degree by the series resistances of solar cell and system. A series resistance of 1 m Ω (the resistance of a 60 cm long Cu wire with 1 mm² cross-section!) can make a difference – and this means that for precise measurements of ‘working’ solar cells, current and voltage leads are needed, correspond-

ing to counter electrode and working electrode for the current, and reference electrode and second reference electrode for the potential in electrochemical terms. A control loop then keeps the potential at the voltage probe at exactly 0 V, independent of the current actually flowing. If measurements at any other points on the $I-V$ characteristic of an (illuminated) solar cell are desired, the hardware setup for driving the solar cell is pretty much the same as for semiconductor photo-electrochemistry. A system meeting these requirements exists: it is known by the acronym CELLO (solar CELl Local Characterization). CELLO has been developed by the Kiel group and is described in a number of publications [62, 63].

In a somewhat simplified view, CELLO by itself allows one to characterize solar cells locally with respect to their ‘electrical’ parameters. In short, an illuminated solar cell of any kind is held at some arbitrary working point with two of the three defining parameters (voltage, current, illumination intensity) held at constant value with high pre-

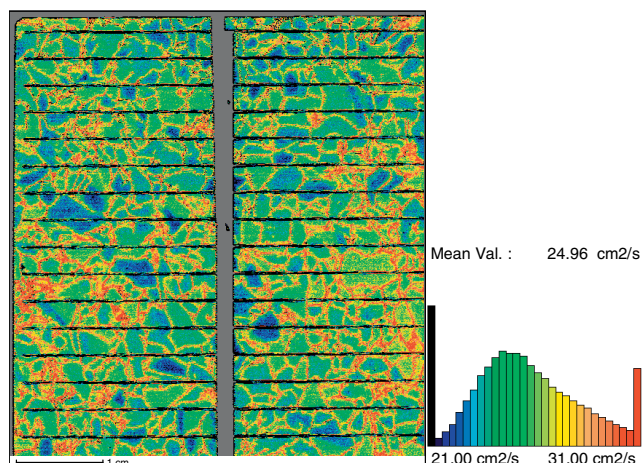


Figure 9 (online colour at: www.pss-a.com) Map of the diffusion coefficient of minority carriers (electrons) and quantitative scale obtained by fsi-PI.

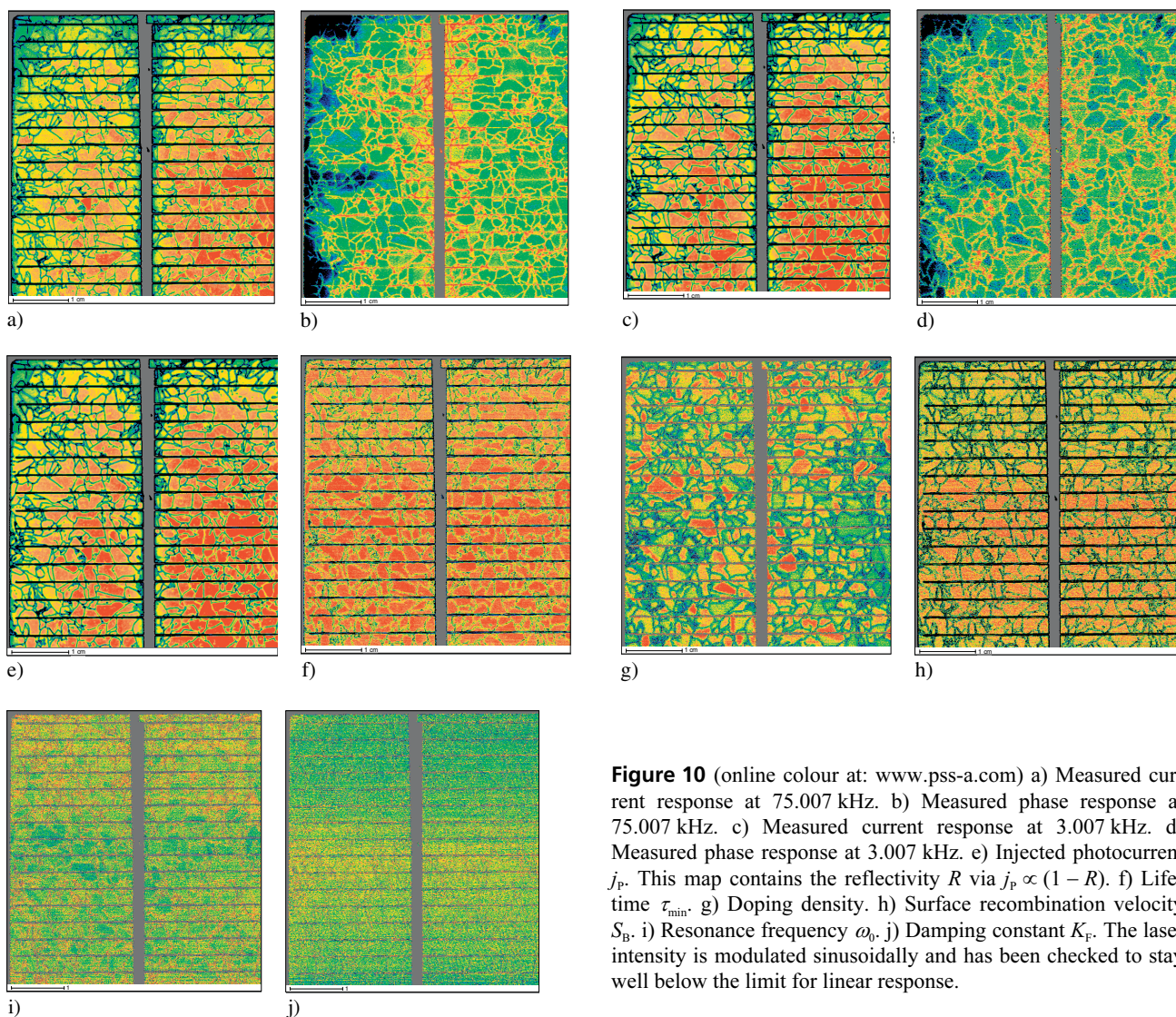


Figure 10 (online colour at: www.pss-a.com) a) Measured current response at 75.007 kHz. b) Measured phase response at 75.007 kHz. c) Measured current response at 3.007 kHz. d) Measured phase response at 3.007 kHz. e) Injected photocurrent j_p . This map contains the reflectivity R via $j_p \propto (1 - R)$. f) Lifetime τ_{\min} . g) Doping density. h) Surface recombination velocity S_B . i) Resonance frequency ω_0 . j) Damping constant K_F . The laser intensity is modulated sinusoidally and has been checked to stay well below the limit for linear response.

cision and minimal drift (via feedback control loops). A laser produces a local disturbance at some selected pixel to which the solar cell can only globally respond by a small change of the free third parameter. Recording the voltage response for 'galvanic' conditions or the current response for 'potentiostatic' conditions at several working points generates a (large and noisy) set of data that are matched to an advanced model of the solar cell (taking into account, for example, lateral current flow via the grid). High-resolution maps (pixel size typically 0.6 mm) of quantities like short circuit current I_{SC} , open circuit voltage U_{OC} , or series and parallel resistances R_{ser} or R_{par} result.

Modulating the laser and adding the information extracted from the resulting impedance data allow one to extend the characterization to the physical quantities encoded in Z_{fsi} as described above. While fitting large amounts of (noisy) data to a highly nonlinear function as given by Eq. (14) is not a simple task, it is 'just' software; how it is done in reality shall not be discussed here.

The application of fsi-PI spectroscopy to solar cells shall be demonstrated for the case of a standard solar cell based on so-called multicrystalline Si taken from current production. Figure 9 shows an example of the full set of data obtained for one of the primary 8 parameters extracted; it is the diffusion coefficient of the *minority* carrier, a quantity that has never been locally measured before. The histogram in the right-hand side fully quantifies the map; note that the mean value of $\langle D \rangle = 25 \text{ cm}^2/\text{s}$ translates into a mobility $\mu = 990 \text{ cm}^2/(\text{V s})$ which is well within the range of values typically found for multicrystalline Si [64].

Figure 10 shows some more of the results obtained for the same standard multicrystalline Si solar cell as in Fig. 9. In order to save space, the histograms are omitted and only the average value of the quantity plotted is given.

More maps than just those for the 8 prime parameters can be obtained; e.g. maps of the doping density (from the D -map), the $R_{ser}C$ time constant, or just for C and R_{ser} . There are several interesting features to observe.

First, it is satisfying to see that the maps of ω_0 and the damping constant K_F show hardly any x, y dependence, as one would expect (note the very small dynamical range in Fig. 10i and j). While these quantities have to be extracted in order to be able to obtain the other ones, they are not of much interest. They indicate that the resonance frequency of the system is around 225 kHz (not a bad value for a high-power potentiostat capable of delivering several amps), and that it is heavily damped, as it should be. One benefit of being able to separate the hardware influence might be that the conditions for hardware design could be relaxed slightly.

The data extracted from fsi-PI for the Si part and for the $R_{ser}C$ part are quite reasonable if compared to that subset of data that could be obtained independently. In the cases where a direct comparison is not possible (there is, for example, no other known method for mapping the diffusion coefficient of minorities or the back-side recombi-

nation velocity quantitatively), the values obtained are well within the bandwidth of expected values. These are first results, however, and it remains to be seen how reliable the procedure will be.

6 Discussion and conclusion We have demonstrated that impedance spectroscopy in different modes can be applied in situ to complex pore growth phenomena observed for InP and for Si, and that it is possible to extract important parameters for pore growth from the data obtained. We have also demonstrated that both the bsi and the fsi mode of PI spectroscopy can be used in this context, but additionally also in the area of solar cell material research and development. A successful application as demonstrated here depends on several critical issues – suitable hardware and software, a reliable FFT technique, suitable modeling of the processes in question, understanding of critical system issues, and handling and processing large amounts of data including involved numerical routines. The potential of this approach is quite large; the results presented just dealt with a few of the many issues in the field of semiconductor electrochemistry and solar cell research and development. More work is needed to assess the potential of the technique, and new questions, some of which are probably not even known at present, will have to be addressed. The following gives a few examples.

A full (at least semiquantitative) understanding of the InP 'curro-crysto puzzle' outlined in Section 3 would be a big step forward for semiconductor electrochemistry. While impedance spectroscopy by itself cannot provide the answer directly, it has been shown that the plethora of data obtained can be of considerable help in conceiving and in testing models.

While pore growth under fsi conditions is not of prime interest, the few investigations undertaken in this direction [65, 66] do pose some interesting questions not yet answered. It is conceivable that the peculiar interaction of (growing) pores and light propagating in the pore direction ('leaky waveguide' concept, given in some detail in [67, 68]) would allow one to obtain interesting fsi-PI spectra, in particular if the wavelength is used as an independent parameter.

So far only macropores have been addressed in all of the above and in the experiments shown. The simple reason for this is that light is generally not needed for the formation of meso- and micropores, or for macropores in p-type Si, limiting impedance spectroscopy to the UI mode. Indeed, conventional impedance spectroscopy has been used in the context of, for example, micropore formation in p-type Si [46] but not much has been learned from this. However, while light is not needed in general, it still may be necessary if n-type Si is used instead of the ubiquitous p-type wafers. While this would be a useless complication if one just wants to produce some microporous Si for whatever purpose, it opens the way to apply PI and UI measurements to some other pore types, too, greatly increasing the analytical power of the method.

In a similar vein, there are few impedance spectroscopy data from whatever mode in the context of pore etching in semiconductors other than Si. A direct transfer of the methodology proposed here, however, is only possible up to a point. Pore etching in these materials might be far more sensitive to experimental conditions like electrolyte flow or sample surface conditions, often leading to very non-uniform pore nucleation. The obvious solution of using lithographically defined nuclei to overcome nucleation problems is, unfortunately, not readily available, and quite often does not work (as far as one can tell from the limited numbers of studies made [9, 69]). Moreover, strong self-organization on various levels (e.g. [70]) tends to obscure the issue even more. Nevertheless, these problems still can be tackled with the approach described here as demonstrated in Section 3, and more effort along these lines might bear rich fruit.

While it might be premature to apply FFT impedance spectroscopy to the growing field of pores or nanotubes produced by anodic oxidation of metals like Al [71] or Ti [72, 73], systematic investigations of just the anodic oxidation of Si (and other semiconductors) are possible; a first step in this direction has been made in [74, 75]. Again, if n-type Si is used, PI modes can be applied in conjunction with UI impedance; whether anything can be learned from this still needs to be determined.

That fsi-PI impedance spectroscopy can be a powerful tool for the mapping (or wholesale measurements) of many interesting properties of solar cells and solar materials is obvious. Using an electrolyte contact instead of a p–n junction is a trivial (if somewhat expensive) problem; e.g. the ELYMAT technique, used for mapping minority carrier lifetimes in Si wafers [58], could also be adopted without any problems to fsi PI. However, the nonlinear matching of up to 11 parameters to (more or less noisy) data is not without pitfalls and risks. A careful evaluation of the range of applicability is needed, ideally culminating in software that recognizes and avoids (or repairs) possible mistakes.

Nevertheless, it can be vouchsafed that the systematic approach to impedance spectroscopy using FFT techniques and utilizing PI wherever possible as has been presented here in the context of semiconductor electrochemistry, while still in its infancy, will in time become a powerful tool that will help in unraveling the many mysteries that still plague the field.

Acknowledgements The authors gratefully acknowledge considerable help and critical comments from Dr G. Popkurov and the able assistance of Mrs Katrin Brandenburg. Parts of this work have been supported by the Alexander von Humboldt Foundation.

References

- [1] J. R. MacDonald, *Impedance Spectroscopy* (John Wiley & Sons, 1987).
- [2] V. Lehmann, *Electrochemistry of Silicon* (Wiley-VCH, Weinheim, 2002).
- [3] X. G. Zhang, *Electrochemistry of Silicon and Its Oxide* (Kluwer Academic/Plenum, New York, 2001).
- [4] L. T. Canham and V. P. Parkhutik (eds.), *phys. stat. sol. (a)* **182**(1), 1–602 (2000).
- [5] L. T. Canham, A. Nassiopoulou, and V. Parkhutik (eds.), *phys. stat. sol. (a)* **197**(1), 9–302 (2003); **197**(2), 311–585 (2003).
- [6] L. T. Canham, A. Nassiopoulou, and V. Parkhutik (eds.), *phys. stat. sol. (a)* **202**(8), 1347–1718 (2005); *phys. stat. sol. (c)* **2**(9), 3185–3512 (2005).
- [7] V. Parkhutik, A. Nassiopoulou, M. Sailor, and L. T. Canham (eds.), *phys. stat. sol. (a)* **204**(5), 1245–1540 (2007); *phys. stat. sol. (c)* **4**(6), 1883–2190 (2007).
- [8] H. Föll, M. Christophersen, J. Carstensen, and G. Hasse, *Mater. Sci. Eng. R* **39**, 93 (2002).
- [9] H. Föll, S. Langa, J. Carstensen, S. Lölkes, M. Christophersen, and I. M. Tiginyanu, *Adv. Mater.* **15**, 183 (2003).
- [10] R. L. Smith and S. D. Collins, *J. Appl. Phys.* **71**, R1 (1992).
- [11] O. Bisi, S. Ossicini, and L. Pavesi, *Surf. Sci. Rep.* **38**, 1 (2000).
- [12] S. Ossicini, L. Pavesi, and F. Priolo, *Light Emitting Silicon for Microphotonics* (Springer, Berlin, 2003).
- [13] V. Lehmann, S. Stengl, and A. Luigart, *Mater. Sci. Eng. B* **69/70**, 11 (2000).
- [14] J.-N. Chazalviel, R. Wehrspohn, and F. Ozanam, *Mater. Sci. Eng. B* **69/70**, 1 (2000).
- [15] S. Keipert, J. Carstensen, and H. Föll, *Electrochem. Soc. Trans.* **6**, 387 (2007).
- [16] C. Fang, H. Föll, and J. Carstensen, *J. Electroanal. Chem.* **589**, 259 (2006).
- [17] J. Li and L. M. Peter, *J. Electroanal. Chem.* **193**, 27 (1985).
- [18] J. Li and L. M. Peter, *J. Electroanal. Chem.* **199**, 1 (1986).
- [19] Y. Stricot, P. Clechet, and J. R. Martin, *Appl. Phys. Lett.* **49**(1), 32 (1986).
- [20] J. N. Chazalviel, *Electrochim. Acta* **33**, 461 (1988).
- [21] L. M. Peter, *Chem. Rev.* **90**, 753 (1990).
- [22] A. R. de Wit, D. Vanmaekelbergh, and J. J. Kelly, *J. Electrochem. Soc.* **139**, 2508 (1992).
- [23] D. Vanmaekelbergh, A. R. de Wit, and F. Cardon, *J. Appl. Phys.* **73**, 5049 (1993).
- [24] S. Krause, W. Moritz, H. Talabani, M. Xu, A. Sabot, and G. Ensell, *Electrochim. Acta* **51**, 1423 (2006).
- [25] E. Foca, J. Carstensen, G. Popkurov, and H. Föll, *Electrochem. Soc. Trans.* **6**, 345 (2007).
- [26] E. Foca, J. Carstensen, G. Popkurov, and H. Föll, *phys. stat. sol. (a)* **204**, 1378 (2007).
- [27] M. Christophersen, S. Langa, J. Carstensen, P. M. Fauchet, and H. Föll, *MRS Proceedings*, Spring Meeting, invited paper (2003).
- [28] J. C. Claussen, J. Carstensen, M. Christophersen, S. Langa, and H. Föll, *Chaos* **13**, 217 (2003).
- [29] ET&TE Etch and Technology GmbH, <http://www.et-te.com>.
- [30] G. S. Popkurov and R. N. Schindler, *Rev. Sci. Instrum.* **63**, 5366 (1992).
- [31] G. S. Popkurov, *Electrochim. Acta* **41**, 1023 (1996).
- [32] G. S. Popkurov and R. N. Schindler, *Electrochim. Acta* **38**, 861 (1993).
- [33] S. Langa, M. Christophersen, J. Carstensen, I. M. Tiginyanu, and H. Föll, *phys. stat. sol. (a)* **197**, 77 (2003).

- [34] A. Hamamatsu, C. Kaneshiro, H. Fujikura, and H. Hasegawa, *J. Electroanal. Chem.* **473**, 223 (1999).
- [35] S. Frey, M. Kemell, J. Carstensen, S. Langa, and H. Föll, *phys. stat. sol. (a)* **202**, 1369 (2005).
- [36] J. Wloka, K. Mueller, and P. Schmuki, *Electrochem. Solid-State Lett.* **8**, B72 (2005).
- [37] E. Spiecker, M. Rudel, W. Jäger, M. Leisner, and H. Föll, *phys. stat. sol. (a)* **202**, 2950 (2005).
- [38] E. Foca, J. Carstensen, and H. Föll, *J. Electroanal. Chem.* **603**, 175 (2007).
- [39] J. Carstensen, M. Christophersen, G. Hasse, and H. Föll, *phys. stat. sol. (a)* **182**, 63 (2000).
- [40] J. Carstensen, M. Christophersen, and H. Föll, *Mater. Sci. Eng. B* **69/70**, 23 (2000).
- [41] P. Russell and J. Newman, *J. Electrochem. Soc.* **133**, 59 (1986).
- [42] M. Keddad, O. R. Mattos, and H. Takenouti, *J. Electrochem. Soc.* **128**, 257 (1981).
- [43] M. Keddad, O. R. Mattos, and H. Takenouti, *J. Electrochem. Soc.* **128**, 266 (1981).
- [44] P. C. Searson and X. G. Zhang, *J. Electrochem. Soc.* **137**, 2539 (1990).
- [45] P. C. Searson and X. G. Zhang, *Electrochim. Acta* **36**, 499 (1991).
- [46] F. Ozanam, J.-N. Chazalviel, A. Radi, and M. Etman, *J. Electrochem. Soc.* **139**, 2491 (1992).
- [47] I. D. Raistrick, *Electrochim. Acta* **35**, 1579 (1990).
- [48] J. Fleig and J. Maier, *Solid State Ion.* **94**, 199 (1997).
- [49] H.-K. Song, Y.-H. Jung, K.-H. Lee, and L. H. Dao, *Electrochim. Acta* **44**, 3513 (1999).
- [50] O. E. Barcia, E. D'Elia, I. Frateur, O. R. Mattos, N. Pebere, and B. Tribollet, *Electrochim. Acta* **47**, 2109 (2002).
- [51] H. K. Song, J. H. Sung, Y. H. Jung, K. H. Lee, L. H. Dao, M. H. Kim, and H. N. Kim, *J. Electrochem. Soc.* **151**, E102 (2004).
- [52] A. Lasia, *J. Electroanal. Chem.* **428**, 155 (1997).
- [53] A. Lasia, *J. Electroanal. Chem.* **500**, 30 (2001).
- [54] E. Foca, J. Carstensen, M. Leisner, E. Ossei-Wusu, O. Riemenschneider, and H. Föll, *Electrochem. Soc. Trans.* **6**, 367 (2007).
- [55] V. Lehmann and H. Föll, *J. Electrochem. Soc.* **137**, 653 (1990).
- [56] S. M. Sze, *Physics of Semiconductor Devices* (Wiley & Sons, New York, 1981).
- [57] H. Föll, *Appl. Phys. A* **53**, 8 (1991).
- [58] J. Carstensen, W. Lippik, and H. Föll, in: *Semiconductor Silicon*, edited by H. R. Huff, W. Bergholz, and K. Sumino (Electrochemical Society, San Francisco, 1994).
- [59] J. Carstensen, W. Lippik, S. Liebert, S. Köster, and H. Föll, in: *Conference proceedings of the 13th European Photovoltaic Solar Energy Conference*, Nice, 1995, p. 1344.
- [60] J. M. Macak, H. Tsuchiya, L. Taveira, S. Aldabergerova, and P. Schmuki, *Angew. Chem.* **117**, 7629 (2005).
- [61] Y. Morishita, S. Kawai, J. Sunagawa, and T. Suzuki, *Electrochem. Solid-State Lett.* **4**, G4 (2001).
- [62] J. Carstensen, G. Popkirov, J. Bahr, and H. Föll, in: *Proceedings of the 16th European Photovoltaic Solar Energy Conf.*, VD3.35, Glasgow (2000).
- [63] J. Carstensen, G. Popkirov, J. Bahr, and H. Föll, *Solar Energy Mater. Solar Cells* **76**, 599 (2003).
- [64] J. Libal, T. Buck, R. Kopecek, P. Fath, K. Wambach, M. Acciarri, S. Binetti, and L. J. Geerlings, in: *Proc. 19th European Photovoltaic Solar Energy Conference*, 2CV.2.45, Paris (2004).
- [65] C. Levy-Clement, A. Lagoubi, and M. Tomkiewicz, *J. Electrochem. Soc.* **141**, 958 (1994).
- [66] T. Osaka, K. Ogasawara, and S. Nakahara, *J. Electrochem. Soc.* **144**, 3226 (1997).
- [67] V. Kochergin, *Omnidirectional Optical Filters* (Kluwer Academic, Boston, MA, 2003).
- [68] V. Kochergin and H. Föll, *Mater. Sci. Eng. R* **52**, 93 (2006).
- [69] H. Föll, S. Langa, J. Carstensen, M. Christophersen, I. M. Tiginyanu, and K. Dichtel, in: *MRS Proceedings Spring Meeting: Materials and Devices for Optoelectronics and Microphotonics*, edited by R. B. Wehrspohn, S. Noda, C. Soukoulis, and R. März, L6.4 (2002).
- [70] H. Föll, J. Carstensen, E. Foca, and M. Leisner, *Electrochem. Soc. Trans.* **6**, 309 (2007).
- [71] O. Jessensky, F. Müller, and U. Gösele, *J. Electrochem. Soc.* **145**, 3735 (1998).
- [72] V. Zwillig, M. Aucouturier, and E. Darque-Ceretti, *Electrochim. Acta* **45**, 921 (1999).
- [73] V. Zwillig, E. Darque-Ceretti, A. Boutry-Forveille, D. David, M. Y. Perrin, and M. Aucouturier, *Surf. Interface Anal.* **27**, 629 (1999).
- [74] M. Leisner, J. Carstensen, and H. Föll, *Electrochem. Soc. Trans.* **6**, 599 (2007).
- [75] M. Leisner, J. Carstensen, and H. Föll, *J. Electroanal. Chem.* **615**, 124 (2008).